OPEN

Fabrication and characterization of monolithically integrated microchannel plates based on amorphous silicon

Andrea Franco, Jonas Geissbühler, Nicolas Wyrsch & Christophe Ballif

Ecole Polytechnique Fédérale de Lausanne (EPFL), Photovoltaics and thin-film electronics laboratory (PV-Lab), Rue de la Maladière 71B, CH-2002 Neuchâtel, Switzerland.

Microchannel plates are vacuum-based electron multipliers for particle—in particular, photon— detection, with applications ranging from image intensifiers to single-photon detectors. Their key strengths are large signal amplification, large active area, micrometric spatial resolution and picosecond temporal resolution. Here, we present the first microchannel plate made of hydrogenated amorphous silicon (a-Si:H) instead of lead glass. The breakthrough lies in the possibility of realizing amorphous silicon-based microchannel plates (AMCPs) on any kind of substrate. This achievement is based on mastering the deposition of an ultra-thick (80–120 µm) stress-controlled a-Si:H layer from the gas phase at temperatures of about 200°C and micromachining the channels by dry etching. We fabricated AMCPs that are vertically integrated on metallic anodes of test structures, proving the feasibility of monolithic integration of, for instance, AMCPs on application-specific integrated circuits for signal processing. We show an electron multiplication factor exceeding 30 for an aspect ratio, namely channel length over aperture, of 12.5 : 1. This result was achieved for input photoelectron currents up to 100 pA, in the continuous illumination regime, which provides a first evidence of the a-Si:H effectiveness in replenishing the electrons dispensed in the multiplication process.

Microchannel plates[1] (MCPs) are well-established electron multipliers that were initially developed for night vision applications and astrophysics[2,3] and progressively spread into different fields such as nuclear[4,5] and plasma[6,7] physics, mass spectrometry[8,9] and biotechnology[10]. Electron multiplication in MCPs takes place inside long thin channels (also called pores), which replace the cascade of discrete dynodes in traditional photomultipliers. Each impinging electron causes the ejection of two or more secondary electrons, which are accelerated and prompt more and more electrons to be ejected, triggering an avalanche effect. The strip current, which flows in a semiconducting layer close to the channel surface, replenishes the lost electrons. A large concentration of channels within one plate provides micrometric resolution over a sensing area of up to several square centimeters[5]. Additionally, electron multiplication in vacuum makes MCPs among the fastest detectors, with raise times below ten picoseconds and dead times (between consecutive detection events and not considering limitations due to the readout technology) on the order of hundreds of picosecond[11,12] (provided that the excitation flux is low enough to prevent the electron multiplication taking place in the same channel at rates larger than its dead time).

The amorphous-silicon-based microchannel plates (AMCPs) presented in this work offer several innovative advantages, which are expected to boost the use of this electron multiplication device.

The first advantage and real breakthrough of AMCPs, which motivated our work, is the possibility to fabricate an AMCP that is vertically integrated either on application-specific integrated circuits (ASICs) or on solid-state detectors. Indeed, the deposition of a-Si:H from the gas phase by plasma-enhanced chemical vapor deposition (PE-CVD) at temperatures of about 200°C can be achieved on nearly any type of substrate and on areas of up to several square meters[13]. Monolithic detectors[14,15] and imaging sensors[16] that feature active layers made of a-Si:H have already been realized, with major improvements such as minimization of the detector dead area, independent optimization of the sensing element and readout electronics, removal of an expensive and complicated bump-bonding technique[16], high level of integration between the sensor and the readout circuit, in-situ data processing and low power consumption.

The second advantage consists of replacing the lead-glass material of conventional MCPs with a-Si:H, a long-established material for applications like photovoltaics[17,18], flat-panel displays[19], X-ray and visible imagers[16] and
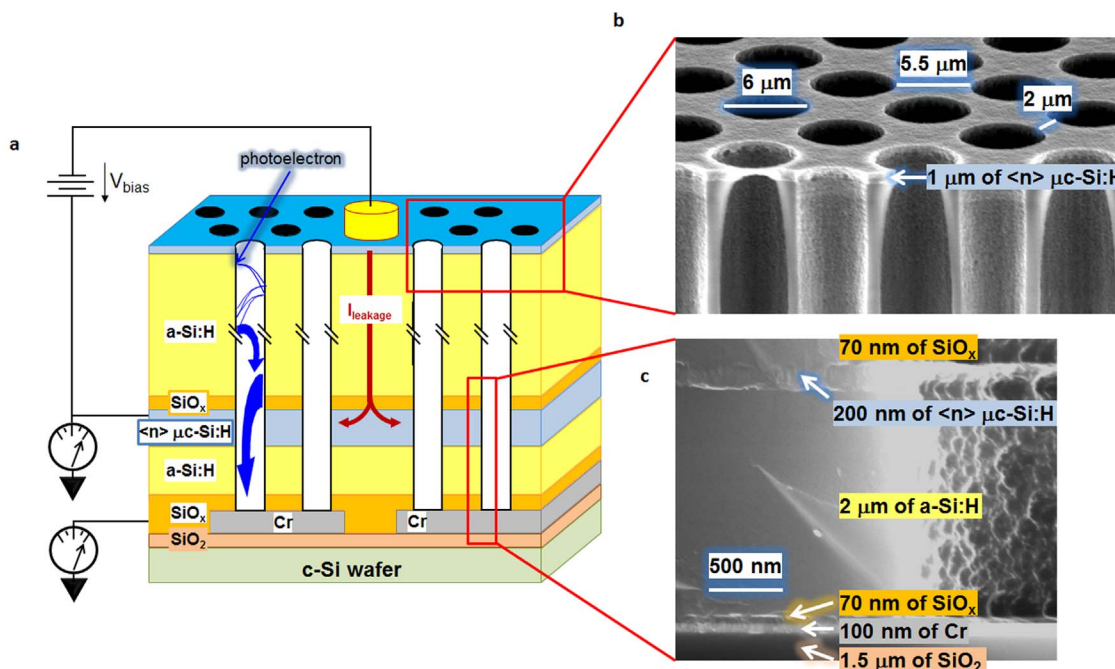
1

Figure 1 | **Vertically integrated AMCP on chromium anodes.** (a) Schematic view of AMCP architecture with channels reaching two independent readout anodes (the two grey layers on oxidized wafer). A bias voltage is applied on the top electrode and leakage currents are evacuated by the intermediate electrode, which is decoupled from the anodes by a 2 μm-thick a-Si:H layer. (b) Cross-sectional SEM image of the top of an AMCP showing the channel geometry. The <n> μc-Si:H electrode can be distinguished from the thick a-Si:H layer by the brighter contrast of its microcrystalline structure. (c) Cross-sectional SEM image of the base of an AMCP with an <n> μc-Si:H intermediate electrode isolated from the chromium anodes by a-Si:H. The two thin SiOx layers, which improve a-Si:H adhesion, have the same morphology as a-Si:H and are barely visible.

particle detectors[15]. The advantage of a-Si:H lies in its bulk resistivity, which is large enough to sustain a high bias voltage and small enough to provide charge replenishment for ejected secondary electrons, without excessive leakage current. This resistivity dispenses with the need for an additional thin semiconducting layer at the channels surface, as in state-of-the-art lead-glass MCPs, to replenish ejected electrons during multiplication.

An additional advantage of AMCPs is that channel micromachining is performed with techniques developed for the microelectronics industry, which allows the channel geometry to be fully customized. The combination of photolithography and deep reactive ion etching (DRIE) can provide aspect ratios comparable to lead-glass MCPs[20].

Our former AMCP prototypes[21] showed an interesting potential, but their characterization was problematic and possible applications scarce. These limitations originated from the device architecture, which needed to be considerably revised. In this work, we detail the fabrication of an upgraded AMCP architecture, which elegantly and effectively surpasses previous limitations. We confirm the successful vertical integration of AMCPs on metallic anodes of test structures, which represents the first step towards monolithic integration on ASICs. We provide the proof of concept with measurements of electron multiplication in the continuous illumination regime. Finally, we present a wide variety of applications that can benefit from vertically integrated AMCPs on ASICs and solid-state detectors.

Results

Vertically integrated AMCPs. The fabrication of AMCPs in a monolithic architecture on readout electrodes (the anodes) requires particular forethought to minimize interference of leakage currents with measurement of electron multiplication. As mentioned before, the replenishment of ejected secondary electrons in conventional MCPs is obtained by a strip current that flows close to the channel surface and is set by a large bias voltage applied across the plate. At

the channel output end, the multiplied electrons are focused on the physically separated grounded anode by a residual electric field, in order to restrain the deterioration of the spatial resolution. In the AMCP architecture, depicted in Figure 1, any kind of gap between the AMCP intermediate electrode—which corresponds to the backside electrode of conventional MCP—and the anode is eliminated by the vertical integration. This entails that AMCP are fabricated on the anode so that a dielectric layer has to be implemented to decouple the AMCP intermediate electrode from the anode. The decoupling effectiveness is maximized by keeping both the intermediate electrode and the anode at ground potential. The leakage current is evacuated by the intermediate electrode and a portion of this current replenishes the ejected secondary electrons.

This architecture outperforms that of former AMCP prototypes[21], which lacked the dielectric layer and had only one grounded electrode for both multiplied electrons collection and leakage current evacuation. Characterization of these prototypes, performed with a pulsed light source and a lock-in amplifier to remove any DC noise due to the leakage current, led to the conclusions that testing capabilities were still limited, measurement incertitude too large, and potential applications scarce or cumbersome.

The improved AMCP architecture and its vertical integration on metallic anodes is sketched in Figure 1a. Scanning electron microscope (SEM) micrographs in Figure 1b and Figure 1c detail the layer morphology and channel geometry in terms of aperture and pitch. The AMCPs are fabricated on metallic patterned anodes, which are deposited on a polished and oxidized crystalline silicon wafer (to simulate an ASIC). In the order of layer deposition, the structure begins with a dielectric layer stack used to decouple the anodes from the grounded (intermediate) electrode. This dielectric stack is formed from an a-Si:H layer deposited on a buffer silicon oxide (SiOx) layer, which improves adhesion. The intermediate electrode is made of a phosphorous-doped (n-doped) microcrystalline silicon layer (<n> μc-Si:H) and evacuates the leakage current. On top of it, another

buffer SiO_x layer improves the adhesion of the main thick a-Si:H layer, which can have large intrinsic stress. Electron multiplication takes place in the channel portion micromachined throughout this a-Si:H layer, which replenishes ejected secondary electrons. The uppermost layer is the top electrode, made of <n> μc-Si:H, to which a bias voltage is applied to set the accelerating field in channels.

The a-Si:H main layer was deposited with thicknesses of 50 to 100 μm (not to scale in Figure 1a) and enabled us to realize AMCPs with aspect ratios between 6.1 : 1 and 12.5 : 1. The deposition parameters were optimized to minimize intrinsic stress, which depends mainly on the temperature and the hydrogen dilution in the gas mixture.

The AMCP top and intermediate electrodes had to be conductive enough to evenly spread the bias voltage on every channel and evacuate leakage currents with minimal voltage drop, respectively. They also had to be compatible with the channel etching process. To keep the process flow simple, <n> μc-Si:H with a resistivity of about 10^{-2} Ω·cm was chosen. For the top electrode, in the absence of other constraints, a thickness of 1 μm was selected, which resulted in a negligible variation of bias voltage up to few centimeters away from the bonding point. The thickness of the intermediate electrode was the result of a compromise between a thin layer for minimal interference with electron multiplication and a thick one for limiting the voltage drop generated by lateral electron movement during their evacuation. Indeed, this voltage drop slightly biases the intermediate electrode with respect to the anode and consequently reduces the decoupling effectiveness, increasing the noise on the anode. An acceptable compromise was achieved with a thickness of 200 nm, corresponding to a sheet resistance of 800 Ω_{sq} and a maximum drop of 1 V (between the intermediate electrode at the channel under test and the ground) when evacuating the largest leakage currents of about 200 μA.

The adhesion buffer layers are made of SiO_x (Figure 1c) with a sub-stoichiometric oxygen content and a thickness of about 70 nm. Their resistivity, two orders of magnitude larger than that of a-Si:H, does not hinder the homogeneous electric field distribution and electron multiplication process due to their limited thickness.

The decoupling layer had to feature sufficiently large resistance for efficient decoupling and had to be compatible with the channel etching process. An a-Si:H layer with a thickness of 2 μm resulted from a trade-off between the decoupling effectiveness, which increased with layer thickness, and the electron multiplication, which could possibly get increasingly clogged as a function of the thickness. Indeed, the ground potential of both the intermediate electrode and anode meant the absence of an accelerating electric field in the bottom part of the channels, which also hindered charge replenishment and possibly resulted in surface charging of the decoupling layer. The a-Si:H thickness of 2 μm was chosen to dampen the leakage current on the anode by about four orders of magnitude, compared to that on the intermediate electrode. The relevant noise (in terms of residual leakage current on the anode) stabilized to a few nanoamperes for an AMCP bias of 500 V, namely for an equivalent electric field of almost 10^5 V/cm.

Chromium was chosen for the anode material because it efficiently acts as an etching-stop layer at the end of the channel micromachining process, it has excellent adhesion properties and a low diffusivity in a-Si:H. It is also easily removed by a selective wet etching process, which allowed us to pattern the chromium layer in a number of independent anodes connected by 100 μm-wide lines to relevant bonding pads.

The crystalline silicon substrate was chosen for its thermal expansion coefficient, which is similar to that of amorphous silicon. Furthermore, its flexibility and ruggedness eased AMCP fabrication. Its passivation with a silicon dioxide (SiO_2) layer of 1.5 μm ensured the electrical isolation of the independent anodes.

All layers other than chromium, which was sputtered, were deposited by PE-CVD (see Methods for further details). Once all deposition steps were completed, the chromium bonding pads were disengaged by reactive ion etching. Eventually, channel apertures between 5 and 7 μm, and pitches between 11 and 13 μm, were defined with lithography and micromachined by DRIE (see Methods for further details), with a maximum aspect ratio of 12.5 : 1. Optimization of both the lithography and etching processes enabled us to obtain cylindrical channels with sharp edges and excellent reproducibility, as shown in Figure 1b.

AMCP test structure. A number of AMCP test structures were realized on the same four-inch wafer. They feature different channel apertures, which correspond to a number of aspect ratios, and different pitches, which correspond to a number of active areas (global AMCP open areas). Each test structure, such as the one shown in Figure 2a, features 21 AMCPs on top of anodes of three different sizes. AMCPs can be recognized as darker squares aligned in two columns and delimited by the rectangular area shown in Figure 2a. A bias voltage is evenly spread to all AMCPs by the <n> μc-Si:H electrode, which is limited to the rectangular area. Indeed, on either side of this area, the stack is progressively removed by dry etching to access the bonding pads.

AMCP characterization setup. In Figure 2b, the test structure is implemented on an interface board for AMCP characterization in a vacuum vessel (Figure 2c). UV photons, provided by a mercury lamp at 254 nm, are converted into photoelectrons by a 16 nm-thick gold photocathode. A screen, made of an aluminum foil with a rectangular hole, is mounted between the photocathode and the AMCP to prevent parasitic photoelectron collection by the bonding wires. The interface board is mounted on a rotating rod that allows the AMCP to be tilted with respect to incoming UV light, so that residual non-converted photons do not influence the measurements. Indeed, the signal was observed to have an additional undesired contribution when photons reached the decoupling layer, because their absorption generated free electron-hole pairs in a-Si:H, which enhanced the material conductivity and reduced the anode isolation. However, as soon as the tilt was large enough to maintain the decoupling layer in dark, no dependency on the illumination was observed on the output signal anymore.

Electron multiplication in AMCPs. The gain, or the number of multiplied electrons per incident photoelectron, is one of the most important MCP parameters and is defined as $G = \delta^n$, where δ is the secondary electron coefficient—namely the number of ejected electrons per impinging electron—and n is the number of collisions. In our work, AMCP gain is measured in a continuous regime within a timeframe of about 4 ms. This corresponds to the frequency of 125 Hz at which a lock-in amplifier drives a mechanical chopper for light modulation, with a duty cycle of 50%. Such measurement technique enables to filter any residual spurious DC contribution, which leaks to the anode. The same gain was confirmed for chopping frequencies between 25 and 425 Hz. Gain is computed as the ratio of signals measured when an AMCP is alternatively biased and grounded. The latter provides the calibration of the photoelectron current into the channels (I_0) because no multiplication occurs with an unbiased AMCP. Both signals are measured as current variations, as shown in Figure 3a, which are induced upon photocathode biasing. Here, it is important to notice that the current measured prior to the photocathode biasing is not representative of the real noise level on the anode, but rather an artifact of the lock-in measurement. Indeed, the measured current depends on the lock-in frequency so that it is likely to be induced by the capacitive coupling between intermediate electrode and anode. However, the gain was confirmed to be independent from the lock-in frequency. The resulting electric field between the photocathode and AMCP is 1250 V/cm. In agreement with the MCP working principle, electron multiplication grows when AMCP bias is increased from 300 to 500 V, as observed in the increasingly larger current variations of Figure 3a.
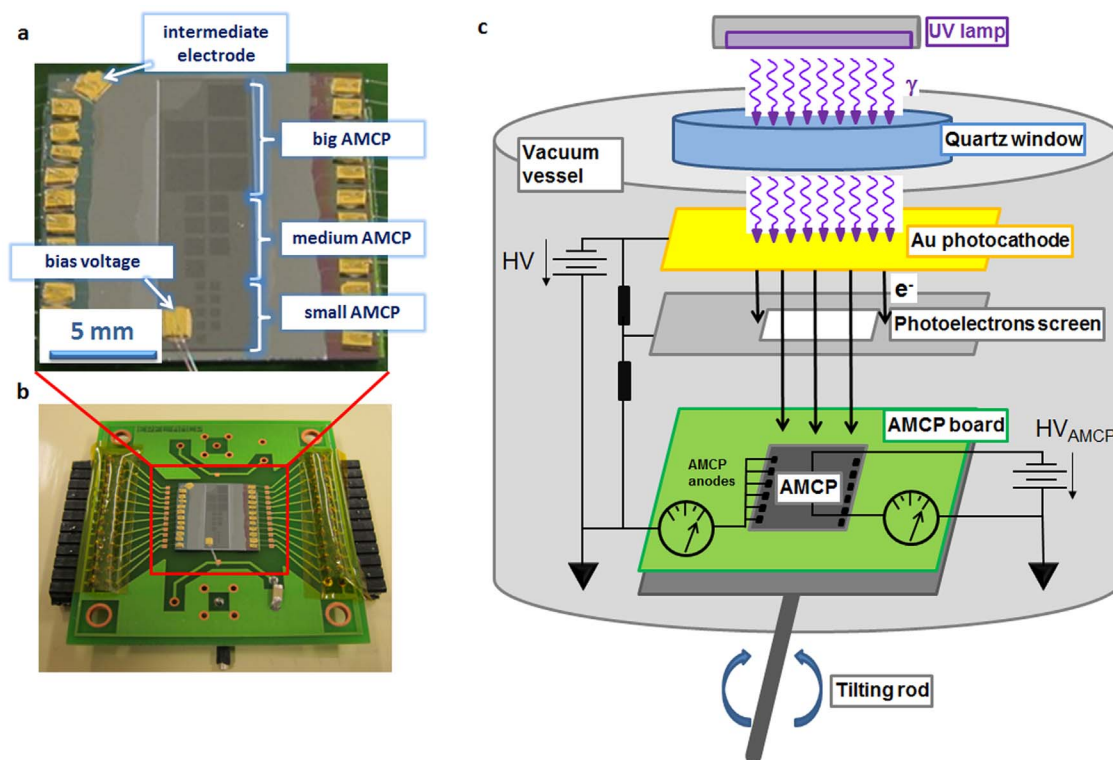
Figure 2 | AMCP test structure, interface board and test setup. (a) A test structure with 21 independent AMCPs—the dark squares in the middle of the structure—vertically integrated on chromium anodes. On either side of the central rectangular area, which corresponds to the full deposited stack, the a-Si:H is progressively etched until the bonding pads are reached. (b) A test structure connected via aluminum wires to the interface board for electrical testing. (c) Schematic representation of the testing configuration inside a vacuum vessel. UV photons enter in vacuum vessel through a quartz window and are converted into photoelectrons the 16 nm-thick gold photocathode evaporated on quartz. The photoelectron screen prevents the parasitic photoelectron absorption by the bonding wires. The tilting rod prevents non-converted photons from reaching the a-Si:H decoupling layer and interfering with the electron multiplication measurements.

The calculated gain for all tested bias voltages is shown in Figure 3b. The largest applied electric field of $6.6 \cdot 10^4$ V/cm (bias voltage of 500 V) yields a gain exceeding 30 for 76 μm-long and 6.1 μm-wide channels, corresponding to an aspect ratio of only 12.5 : 1. Furthermore, we believe that the gain is underestimated to a certain extent because we assume that all the electrons that get inside the channels (I_0) are multiplied, which is most likely not case for non-tilted channels.

The same AMCP gain values are measured for four input photo-electrons currents (I_0). Remarkably, no gain dampening is observed for I_0 above 90 pA, which provides a first evidence of the effectiveness in the charge replenishment mechanism (due to the a-Si:H bulk conductivity) of AMCPs. Additionally, a comparable gain at different I_0 proves that the possible charging of the decoupling layer did not constitute a problem so far. It is worth to mention that the AMCP was not tested above the maximum value of 93 pA because of
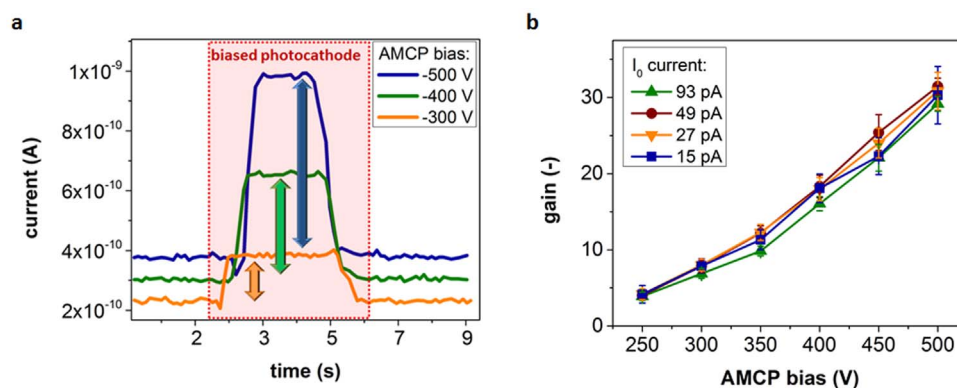

Figure 3 | Electron multiplication in an AMCP. (a) Current measured on the anode, which increases abruptly upon photocathode biasing due to the acceleration of photoelectrons towards the AMCP and their subsequent multiplication in it. The larger the AMCP bias, the larger the electron multiplication, as is shown by the vertical arrows referring to voltages between −300 and −500 V. (b) The gain grows steadily with bias voltage up to −500 V, at which point it exceeds 30 for an aspect ratio of only 12.5 : 1. The gain values are comparable for different input photoelectron currents, which indicate the effectiveness of charge replenishment in the AMCP.
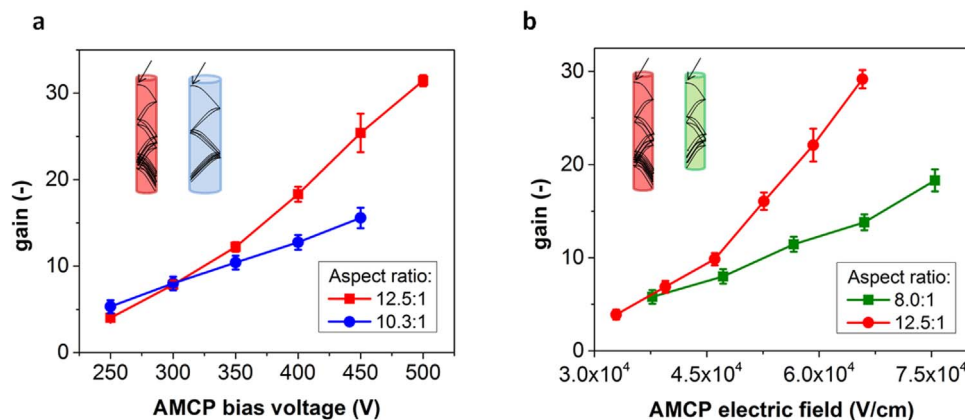
Figure 4 | AMCP gain dependency on aspect ratio. (a) Gain versus bias voltage at $I_0 = 93$ pA for aspect ratios of 10.3 : 1 and 12.5 : 1, with a channel length of 76 μm and channel apertures of 7.6 and 6.1 μm, respectively. (b) Gain versus electric field at $I_0 = 93$ pA for aspect ratios of 12.5 : 1 and 8 : 1, with a channel aperture of 6.1 μm and channel lengths of 76 and 53 μm, respectively. The electric field, rather than the bias voltage, is plotted on the x-axis to compare AMCPs with different channel lengths.

the limitation of the photocathode response to the adopted wavelength. The maximum bias voltage was limited to 500 V to avoid the risk of breakdown induced by the electric field.

AMCP gain dependency on aspect ratio. The electron multiplication mechanism in MCPs is enhanced by large aspect ratios because longer channels and smaller apertures entail more collisions. This dependency is confirmed for AMCPs as well, which gives additional confirmation about the electron multiplication. Figure 4a shows gain curves for aspect ratios of 10.3 : 1 and 12.5 : 1, corresponding to channel apertures of 7.4 and 6.1 μm, respectively. The gain is plotted as a function of bias voltage because both AMCPs have the same channel length of 76 μm and, therefore, the same accelerating electric field for a given bias. The larger gain for the aspect ratio of 12.5 : 1 is explained by shorter trajectories in narrower channels, corresponding to more collisions.

Figure 4b compares the gain of a third AMCP with an aspect ratio of 8 : 1 to the 12.5 : 1 AMCP. As expected, the smaller-aspect-ratio AMCP, with the same aperture but a shorter channel length of 53 μm, exhibits a lower gain. In this second graph, the electric field has replaced bias voltage on the x-axis, to compare gain results in the same accelerating field.

Discussion

The results show a gain that grows as a function of bias voltage and aspect ratio, consistent with the MCP working principle. The modest measured gain values, compared to conventional MCPs, are evidently related to small aspect ratios. These gain values hindered a more comprehensive characterization, which could not encompass pulse height distribution, response time, dead time, and background rate. Nonetheless, the AMCP gain curves can be analyzed to extract important parameters about the multiplication process, like the number of collisions, which is to say, the number of equivalent discrete dynodes. In a model developed by Eberhardt[22], the number of collisions can be obtained from the slope of the linear regression curve performed on the logarithm of gain versus the logarithm of bias voltage. Although Eberhardt's model makes the strong assumption that the number of collisions is independent of the bias voltage, it can nevertheless be exploited to compare AMCPs and conventional MCPs in terms of number of collisions versus aspect ratio. The applicability of the model to AMCPs is confirmed by the linearity of the gain curves as a function of bias voltage in a fully logarithmic plot. This is shown in Figure 5a, where the three aspect ratios presented above are plotted together with a fourth set of data for an AMCP with an aspect ratio of 6.1 : 1. The number of collisions is
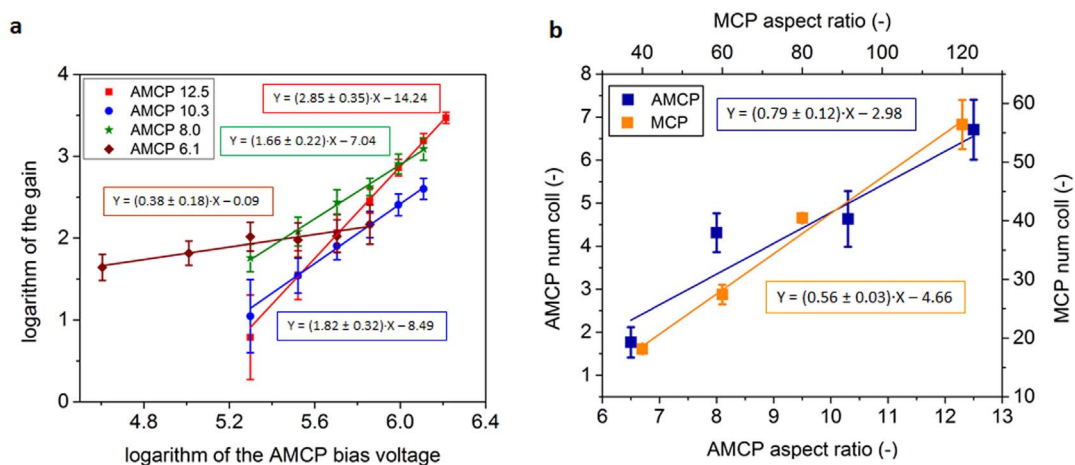

Figure 5 | Number of collisions versus aspect ratio for AMCPs and conventional MCPs. (a) Logarithm of AMCP gain versus logarithm of bias voltage for all realized aspect ratios from 6.1 to 12.5. The slopes of the linear regression curves can provide insight about electron multiplication, as they are proportional to the number of collisions, according to Eberhardt[22]. (b) Calculated number of collisions versus aspect ratio for AMCPs and conventional MCPs[22]. Linear regression curves give an estimate of the number of collisions as a function of aspect ratio.

obtained by dividing the slopes of linear regression curves by a factor that relates the secondary electron coefficient with the electron kinetic energy. Although this factor varies significantly in the literature[23], we chose Eberhardt's value of 0.5 for comparing our AMCPs to his data on conventional MCPs[22]. The results are shown in Figure 5b. The calculated slopes are 0.79 ± 0.12 for AMCPs and 0.56 ± 0.03 for MCPs. The small mismatch in slopes could be explained by the small number of collisions taking place in the AMCPs, given their modest aspect ratios, for which the model may not be valid anymore. Indeed, the assumption that the number of collisions is independent of bias voltage may no longer be acceptable for the tested AMCP aspect ratios. However, the mismatch could also be caused by the small number of data points. When one excludes the AMCP with an aspect ratio of 8, the match is indeed excellent.

Besides the mismatch, which is going to be investigated with further data from AMCPs of various (including larger) aspect ratios, the dependency of AMCP electron multiplication on aspect ratio is similar to that of conventional MCPs. Additionally, according to the a-Si:H secondary electron yield of 1.5–1.7, inferred from the dependency of electron multiplication versus number of collisions, we expect the gain to increase by a factor 10^2–10^3 for an aspect ratio of 30 : 1. This is a reasonable goal considering our improvements about stress-controlled a-Si:H deposition and the optimization of the DRIE process. Another gain enhancement is expected by the atomic layer deposition of a high secondary-emission material like alumina (Al_2O_3), as it was successfully achieved in conventional MCPs[24]. We also aim at the improvement of the decoupling layer in terms of reduction of the leakage current reaching the anode, which presently corresponds to a noise of about 1–10 pA. This goal will be attained by depositing more-resistive a-Si:H, which can be achieved, for instance, by adding a gas precursor containing carbon like carbon dioxide (CO_2). The presence of carbon in a-Si:H induces a widening of the a-Si:H forbidden gap and makes the material more resistive. Consequently, the resistivity is expected to increase by about two orders of magnitude. This achievement will also permit us to reduce the thickness of the decoupling layer, in order to minimize possible interferences to the electron multiplication produced by surface charging. Both the larger gain and the enhanced anode isolation are going to increase the AMCP sensitivity to input intensities lower than the present 1 pA, aiming at photon counting applications.

As far as characterization is concerned, an AMCP will be tested in photon counting mode by placing one or two conventional MCPs above it so that the total gain is boosted and the AMCP pulse height distribution (PHD) can be extracted. The PHD curve will be used to gain further insights about the dynamics of electron multiplication, possible limitations and indications for further structural improvements.

Ultimately, the vertical integration of AMCPs on real readout electronics like Medipix2[25] ASIC will yield the first monolithic detector featuring a microchannel plate. Characterization will then focus on spatial resolution and dynamic range, which is expected to reach the gigahertz range thanks to parallel pixel operation.

To conclude, we have successfully fabricated and upgraded the first microchannel plate made of amorphous silicon. This material has proven to be an excellent choice for an application where large bias voltages are required, on the one hand, and sufficient conductivity to replenish ejected charges is essential, on the other. We showed how processes of the microelectronic industry can be successfully employed to fabricate AMCPs, whose channel geometry can be easily customized. We provided the proof of concept for AMCPs by achieving a promising gain value above 30 for an aspect ratio of 12.5 : 1. We also believe that this gain was underestimated to a certain extent because, in the gain calculation, we assumed that all photoelectrons entering in the channels were multiplied, which is not necessarily the case for non-tilted channels. We are currently investigating this matter by testing AMCP with an electron gun, which

allows us to tilt the AMCP with respect to the direction of incoming electrons. First results seem to confirm that the gain was actually underestimated of at least a factor two.

We gave first evidence that the choice of a-Si:H as the bulk material can efficiently sustain the multiplication and avoid gain saturation for input photoelectron currents above 90 pA, in the continuous illumination regime. However, given the actual modest gain, these preliminary results will have to be supported by others obtained with AMCP of larger gain and with larger input currents to accurately determine the a-Si:H effectiveness to the charge replenishment.

We demonstrated the feasibility of integrating AMCPs monolithically on readout electrodes, paving the road to a new variety of applications and broadening existing ones. Particle trackers and photon-counting imagers could feature a vertically integrated AMCP on readout electronics developed for nuclear physics, like Medipix2[25–27] and NINO[28,29]. Hybrid detectors[30] with AMCPs on solid-state detectors, like the Geiger-mode avalanche photodiode (G-APD)[30–32], could take advantage of a double multiplication mechanism in a very compact and magnetic-insensitive design. These could be used in applications where both single-photon sensitivity and high temporal resolution are required, like simultaneous positron emission tomography and magnetic resonance imaging[33,34], today's hot topic in medical diagnostic. Finally, an AMCP vertically integrated on charge-coupled arrays (CCDs) could provide a variant of electron-bombarded CCD[35,36] (ebCCD) to be used in single-molecule spectroscopy[10,37] or mass spectrometry[9].

Methods

AMCP layer deposition. All AMCPs presented and measured in this work were deposited on 4-inch single-side-polished 500-μm-thick crystalline silicon wafers. In order to have an insulating substrate, a 1.5-μm-thick SiO_2 layer was grown by thermal oxidation.

Non-intentionally doped a-Si:H was deposited by PE-CVD in a custom-built capacitively coupled reactor. The gas precursors were silane (SiH_4) and hydrogen (H_2) with a flux ratio of 2.9 : 1. The deposition frequency was 70 MHz, the power density 0.05 W/cm², and the pressure 625 μbar. The temperature for the first hour was 205°C and it was eventually raised to 215°C to limit the intrinsic tensile stress whilst ensuring a good material quality. The deposition rate was about 17 Å/s. Deposition of a-Si:H layers with thicknesses of up to 120 μm was achieved in the framework of this work.

The <n> μc-Si:H layer was deposited with the following gas precursors and relevant flows: SiH_4 (2 sccm) and H_2 (98 sccm, of which 10 sccm were mixed with a phosphine content of 0.1%). The power density was 0.025 W/cm², the pressure 450 μbar, and the deposition rate 1.1 Å/s. A sheet resistance of 800 Ω_{sq} was been measured with four-point resistance measurements.

The non-intentionally doped SiO_x layer was deposited with SiH_4 (2 sccm), H_2 (98 sccm) and CO_2 (4 sccm). The power density was 0.045 W/cm², the pressure 700 μbar, and the deposition rate 1.7 Å/s.

Chromium was sputtered from a metallic target with Ar ions at a pressure of $5.5 \cdot 10^{-3}$ mbar. The plasma power was 500 W, and the deposition rate 60 Å/s.

Photolitography and reactive ion etching. The first lithography for the patterning of the chromium electrode was done with AZ1518 resist, spun at 4000 rpm. It was exposed to 55 mJ/cm² and developed with AZ351b 1 : 4 for one minute. The chromium was then etched with a cerium acid solution.

The second lithography was for the mesa patterning, namely to create "islands" where channels were eventually micromachined, and to reach Cr bonding pads by. The dry etching was done with the sulfur hexafluoride (SF_6) gas plus oxygen. It was done with AZ9260 resist, spun at 1000 rpm, exposed to 800 mJ/cm² and developed with AZ400 1 : 4 for nine minutes.

The third lithography was for flattening the wafer surface, which now features 60-to-100-μm-thick a-Si:H "islands", prior to the spinning of the last photolithography resist. The third resist was AZ125nxt, spun at 1900 rpm, exposed to 2000 mJ/cm² and developed with AZ351 1 : 1 for two to three minutes. The last photolithography patterned channel diameters and pitches. It was done with AZ9260 resist, spun at 3600 rpm, exposed to 300 mJ/cm² and developed with AZ400 1 : 4 for five minutes.

Channels were micromachined by DRIE with the Bosch process, in which SF_6 etching was alternated with the deposition of a passivation layer. By repeating these two steps many times, the etching profile did not widen laterally so that high aspect ratios were realized.

Finally, the whole wafer was protected by a resist and eventually diced to separate test structures.

All resists were stripped with acetone.

SEM images of AMCP cross sections (Figure 1b and Figure 1c) were obtained from particular structures, which were realized on the same four-inch wafer and eventually cleaved to investigate and improve the fabrication process.

AMCP bonding on test structures and characterization. Gold pads were glued with a two- component silver paste on Cr bonding pads of AMCP test structures (Figure 2a). The ultrasonic bonding between the AMCP test structure and interface board was done via aluminum wires (Figure 2b). The interface board was mounted on a tilting support that allows the AMCP to be tilted with respect to incoming UV light (Figure 2c). The photocathode was made of a 16-nm-thick gold layer evaporated onto a piece of quartz glass (Figure 2c). The electron screen was a 500-nm-thick aluminum sheet with a 4×8 mm^2 hole in the middle. The photon source was a mercury vapor lamp with its main emission at 254 nm. UV photons entered the vacuum vessel through a fused silica window. The illumination intensity was reduced with a diaphragm and shadowing filters to provide a number of photoelectron currents at the AMCP top electrode. The high photocathode voltage was provided by a SRS310 power supply and a portion of this voltage was also provided to an electrode screen by means of a voltage divider. Photoelectrons were accelerated towards the AMCP by an electric field of 10^3 V/cm. The high AMCP voltage was supplied by a Keithley 487 picoammeter/voltage source, which also measured the AMCP leakage current. Electron multiplication was measured with either a Keithley 617 electrometer or an SR830 lock-in amplifier combined with a mechanical chopper at a frequency of 125 Hz.

1. Ladislas Wiza, J. Microchannel plate detectors. *Nucl. Instr. Meth.* **162**, 587–601 (1979).
2. Siegmund, O., Malina, R., Coburn, K. & Werthimer, D. Microchannel plate EUV detectors for the Extreme Ultraviolet Explorer. *IEEE Trans. Nucl. Sci.* **31**, 776–779 (1984).
3. Fraser, G., Barstow, M., Whiteley, M. & Wells, A. Enhanced soft x-ray detection efficiencies for imaging microchannel plate detectors. *Nature* **300**, 509–511 (1982).
4. Va'Vra, J., Ertley, C., Leith, D., Ratcliff, B. & Schwiening, J. A high-resolution TOF detector—A possible way to compete with a RICH detector. *Nucl. Instrum. Methods Phys. Res. A* **595**, 270–273 (2008).
5. Siegmund, O. *et al.* Novel large format sealed tube microchannel plate detectors for Cherenkov timing and imaging. *Nucl. Instrum. Methods Phys. Res. A* **639**, 165–168 (2011).
6. Kempenaars, M. *et al.* Enhancement of the JET edge LIDAR Thomson scattering diagnostic with ultrafast detectors. *Rev. Sci. Instrum.* **79**, 10E728-710E728-724 (2008).
7. Giudicotti, L. & Pasqualotto, R. Characterization of fast microchannel plate photomultipliers for the ITER core LIDAR Thomson scattering system. *J. Instrum.* **7**, C02037 (2012).
8. Barnes IV, J. H. & Hieftje, G. M. Recent advances in detector-array technology for mass spectrometry. *Int. J. Mass Spectrom.* **238**, 33–46 (2004).
9. Hadjar, O., Fowler, W. K., Kibelka, G. & Schnute, W. C. Preliminary demonstration of an IonCCD as an alternative pixelated anode for direct MCP readout in a compact MS-based detector. *J. Am. Soc. Mass Spectrom.* **23**, 418–424 (2012).
10. Michalet, X. *et al.* Detectors for single-molecule fluorescence imaging and spectroscopy. *J. Mod. Opt.* **54**, 239–281 (2007).
11. Tremsin, A. S. *et al.* High resolution photon counting detection system for advanced inelastic X-ray scattering studies. *IEEE Trans. Nucl. Sci.* **54**, 706–709 (2007).
12. Fraser, G. The gain, temporal resolution and magnetic-field immunity of microchannel plates. *Nucl. Instrum. Methods Phys. Res. A* **291**, 595–606 (1990).
13. Strobel, C., Zimmermann, T., Albert, M., Bartha, J. & Kuske, J. Productivity potential of an inline deposition system for amorphous and microcrystalline silicon solar cells. *Sol. Energ. Mat. Sol.* **93**, 1598–1607 (2009).
14. Franco, A., Riesen, Y., Despeisse, M., Wyrsch, N. & Ballif, C. High Spatial Resolution of Thin-Film-on-ASIC Particle Detectors. *IEEE Trans. Nucl. Sci.* **59**, 2614–2621 (2012).
15. Despeisse, M. *et al.* Hydrogenated amorphous silicon sensor deposited on integrated circuit for radiation detection. *IEEE Trans. Nucl. Sci.* **55**, 802–811 (2008).
16. Lule, T., Schneider, B. & Bohm, M. Design and fabrication of a high-dynamic-range image sensor in TFA technology. *IEEE J. Solid-State Circuits* **34**, 704–711 (1999).
17. Shah, A., Torres, P., Tscharner, R., Wyrsch, N. & Keppner, H. Photovoltaic technology: the case for thin-film solar cells. *Science* **285**, 692–698 (1999).
18. Rech, B. & Wagner, H. Potential of amorphous silicon for solar cells. *Appl. Phys. A Mater. Sci.* **69**, 155–167 (1999).
19. Nathan, A. *et al.* Amorphous silicon thin film transistor circuit integration for organic LED displays on glass and plastic. *IEEE J. Solid-State Circuits* **39**, 1477–1486 (2004).
20. Marty, F. *et al.* Advanced etching of silicon based on deep reactive ion etching for silicon high aspect ratio microstructures and three-dimensional micro-and nanostructures. *Microelectr J.* **36**, 673–677 (2005).
21. Franco, A. *et al.* Amorphous silicon-based microchannel plates. *Nucl. Instrum. Methods Phys. Res. A* **695**, 74–77 (2012).
22. Eberhardt, E. H. An operational model for microchannel plate devices. *IEEE Trans. Nucl. Sci.* **28**, 712–717 (1981).
23. Eberhardt, E. H. Gain model for microchannel plates. *Appl. Opt.* **18**, 1418–1423 (1979).
24. Mane, A. U. *et al.* An atomic layer deposition method to fabricate economical and robust large area microchannel plates for photodetectors. *Phys. Procedia* **37**, 722–732 (2012).
25. Llopart, X., Campbell, M., Dinapoli, R., San Segundo, D. & Pernigotti, E. Medipix2: a 64-k pixel readout chip with 55-µm square elements working in single photon counting mode. *IEEE Trans. Nucl. Sci.* **49**, 2279–2283 (2002).
26. Chmeissani, M. *et al.* First experimental tests with a CdTe photon counting pixel detector hybridized with a Medipix2 readout chip. *IEEE Trans. Nucl. Sci.* **51**, 2379–2385 (2004).
27. Vallerga, J., McPhate, J., Tremsin, A. & Siegmund, O. Optically sensitive MCP image tube with a Medipix2 ASIC readout. *Proc. SPIE* **7021**, 702115 (2008).
28. Anghinolfi, F. *et al.* NINO: an ultra-fast and low-power front-end amplifier/discriminator ASIC designed for the multigap resistive plate chamber. *Nucl. Instrum. Methods Phys. Res. A* **533**, 183–187 (2004).
29. Despeisse, M. *et al.* Low-Power Amplifier-Discriminators for High Time Resolution Detection. *IEEE Trans. Nucl. Sci.* **56**, 375–381 (2009).
30. D'Ambrosio, C. & Leutz, H. Hybrid photon detectors. *Nucl. Instrum. Methods Phys. Res. A* **501**, 463–498 (2003).
31. Joram, C., Rudge, A. & Séguinot, J. Proof of principle of G-APD based hybrid photodetectors. *Nucl. Instrum. Methods Phys. Res. A* **621**, 171–176 (2010).
32. Haba, J. Status and perspectives of pixelated photon detector (PPD). *Nucl. Instrum. Methods Phys. Res. A* **595**, 154–160 (2008).
33. Judenhofer, M. S. *et al.* Simultaneous PET-MRI: a new approach for functional and morphological imaging. *Nat. Med.* **14**, 459–465 (2008).
34. Schlemmer, H.-P. W. *et al.* Simultaneous MR/PET imaging of the human brain: Feasibility study. *Radiology* **248**, 1028–1035 (2008).
35. Cianfarani, C. *et al.* A high-resolution detector based on liquid-core scintillating fibres with readout via an electron-bombarded charge-coupled device. *Nucl. Instrum. Methods Phys. Res. A* **339**, 449–455 (1994).
36. Benussi, L. *et al.* A multichannel single-photon sensitive detector for high-energy physics: the megapixel EBCCD. *Nucl. Instrum. Methods Phys. Res. A* **442**, 154–158 (2000).
37. Roy, R., Hohng, S. & Ha, T. A practical guide to single-molecule FRET. *Nat. Methods* **5**, 507–516 (2008).

Acknowledgments

Author contributions

A.F. coordinated the work, did most of the AMCP fabrication, and conceived and performed the AMCP characterization. J.G. performed and optimized the photolithography. N.W., inventor of AMCP, led the funding project and supervised the work together with C.B.

Additional information

Competing financial interests: The authors declare no competing financial interests.

How to cite this article: Franco, A., Geissbühler, J., Wyrsch, N. & Ballif, C. Fabrication and characterization of monolithically integrated microchannel plates based on amorphous silicon. *Sci. Rep.* **4**, 4597; DOI:10.1038/srep04597 (2014).